Measurement 259 (2026) 119706

Contents lists available at ScienceDirect

Measurement

journal homepage: www.elsevier.com/locate/measurement

Frequency-domain analysis of voltammetric signals: a framework to augment electrochemical sensing explored through benzenediol detection

Abhilash Krishnamurthy [a,b,*], Kristina Žagar Soderžnik [a,b]

[a] Department for Nanostructured Materials, Jožef Stefan Institute, Jamova Cesta 39, 1000 Ljubljana, Slovenia
[b] Jožef Stefan International Postgraduate School, Jamova Cesta 39, 1000 Ljubljana, Slovenia

ARTICLE INFO

Keywords:
Frequency domain
Spectral decomposition
Fourier analysis
Voltammetry
Electrochemical sensors
Benzenediols

ABSTRACT

Electrochemical signals are traditionally interpreted in the time domain, where overlapping faradaic and non-faradaic currents, noise, and drift obscure frequency-dependent behaviour. This study introduces a frequency-domain framework that complements time-domain analysis by decomposing voltammetric signals into their harmonic components through Fourier methods.

AC voltammetry provides experimental evidence of how increasing excitation frequency progressively suppresses faradaic clarity, while a modified Randles equivalent circuit model explains this response through the interplay of charge-transfer, diffusion, and double-layer charging processes. Fourier series analysis of canonical voltammetric techniques, including linear sweep, cyclic, differential pulse, and square wave voltammetry, shows that waveform geometry uniquely defines harmonic structure. Fast Fourier transform analysis of practical data reveals artefacts introduced by finite sampling, binning, and spectral leakage. These effects highlight the need for conceptual awareness when interpreting experimental spectra. Quantitative spectral descriptors such as the centroid, bandwidth, flatness, and low-frequency power fraction link waveform design directly to faradaic visibility and measurement clarity.

Frequency-domain analysis therefore establishes that electrochemical measurement is inherently frequency-structured. By combining experimental data, equivalent circuit modelling and spectral metrics within a single framework, this approach provides a general route to optimise waveform parameters, reduce capacitive interference, and improve interpretability across electrochemical techniques. Viewed more broadly, this perspective reframes the process of the measurement itself, showing that time-domain signals are projections of an underlying spectral reality.

1. Introduction

Electrochemical measurements translate interfacial redox processes into electrical signals. Conventional voltammetric techniques [1] such as chronoamperometry, linear sweep (LSV), cyclic (CV) [2], differential pulse (DPV) [3], and square wave voltammetry (SWV) [4] are interpreted in the time domain [5], where currents are plotted as functions of time or potential. Although straightforward and intuitive, this representation conceals how electrochemical systems respond to excitation frequency. Faradaic and non-faradaic [6] currents overlap in time, while external variables such as drift and noise further obscure their independent contributions [7].

To visualise this hidden dimension, the present study applies AC voltammetry (ACV) [8] to examine the frequency response [9] of an electrochemical sensor based on 20 wt% Pt/C-modified Metrohm DS150 screen-printed electrodes. The electrode platform, previously optimised for benzenediol detection [hydroquinone (HQ), catechol (CC), and resorcinol (RS)], provides a reproducible and well-characterised system in which faradaic and capacitive processes can be observed simultaneously. By superimposing a small sinusoidal perturbation onto a linear potential sweep, ACV reveals how increasing excitation frequency progressively boosts capacitive currents and diminishes faradaic clarity. These experimental observations form the empirical foundation of the frequency-domain framework developed in this work.

The observed trends are rationalised using a modified Randles equivalent circuit, which serves as the mathematical scaffold for interpreting frequency-dependent electrochemical behaviour. The circuit partitions the system into discrete elements representing charge

* Corresponding author at: Department for Nanostructured Materials, Jožef Stefan Institute, Jamova Cesta 39, 1000 Ljubljana, Slovenia.
E-mail address: abhilash.krishnamurthy@ijs.si (A. Krishnamurthy).

https://doi.org/10.1016/j.measurement.2025.119706
Received 17 June 2025; Received in revised form 21 October 2025; Accepted 10 November 2025
Available online 12 November 2025

transfer, diffusion, and double-layer charging, linked through the solution resistance. This abstraction layer explains the competing influences of faradaic and capacitive processes independent of specific analytes and their unique redox mechanisms, and predicts the same frequency-dependent trends evident in the ACV data.

Building on these results, the framework is extended through Fourier [10] and spectral [11] analysis of canonical voltammetric waveforms. Fourier decomposition demonstrates that each technique (LSV, CV, DPV, and SWV) has a distinct harmonic [12] signature dictated by its waveform geometry. Comparing their spectra unifies these methods within a single analytical language, showing how waveform design and parameter selection govern frequency content and consequently the quality of electrochemical signals.

This approach differs fundamentally from electrochemical impedance spectroscopy (EIS) [13], which probes steady-state systems under small perturbations. Here, frequency-dependent behaviour is analysed under dynamic scanning conditions, representative of real voltammetric operation. The emphasis is therefore metrological rather than analytical: the study characterises the structure of electrochemical signals rather than the selectivity, sensitivity, or detection limits for the analytes, which have been reported previously for the same benzenediol system [14].

This study follows a reverse-signal logic: integrating experimental ACV data, mathematical interpretation via the Randles circuit, and spectral generalisation through Fourier analysis to reveal that electrochemical measurement is inherently frequency-structured. The resulting framework provides a practical route to tune waveform parameters, minimise capacitive noise, and improve interpretability across multiple voltammetric techniques. The analysis mirrors this logic in practice, tracing the signal path in reverse: from the measured output (ACV spectra), through the system response (Randles circuit), to the input design (waveform spectra). Fig. 1 (Graphical Abstract) schematically presents a general overview of Fourier analysis.

2. Foundations of Fourier analysis in electrochemical signal decomposition

The Supplementary Information provides a brief theoretical exposition of the Fourier series and Fourier transforms. This section outlines the mathematical framework with Eqs. S1 through S10 offering a step-by-step description of the essentials. These formulae elucidate the decomposition of periodic and aperiodic functions into their constituent frequency components, thereby offering insight into the analytical methods used.

The Supplementary Information also examines the harmonic decomposition of several commonly used waveforms, including the square wave, triangular wave, sawtooth wave, and pulse train. This analysis explores the harmonic content characteristic of each waveform illustrating how specific frequency components shape their unique time-domain profiles. Additionally, the rate at which harmonic amplitudes decay with increasing frequency index is discussed, providing insight into the spectral richness or smoothness of each waveform type.

Fig. 2 illustrates the process of spectral resolution via Fourier analysis. Any periodic waveform in the time domain is the sum of sinusoidal components, each characterised by a distinct frequency and amplitude. By extracting and plotting these amplitudes against their respective frequencies, we obtain the spectrum of the original signal. One can visualise this transformation geometrically in three dimensions, with time on the x-axis, amplitude on the y-axis, and frequency on the z-axis. Projecting this representation onto the time–amplitude (xy) plane retrieves the original waveform, while projection onto the frequency-amplitude (yz) plane reveals its spectral composition.

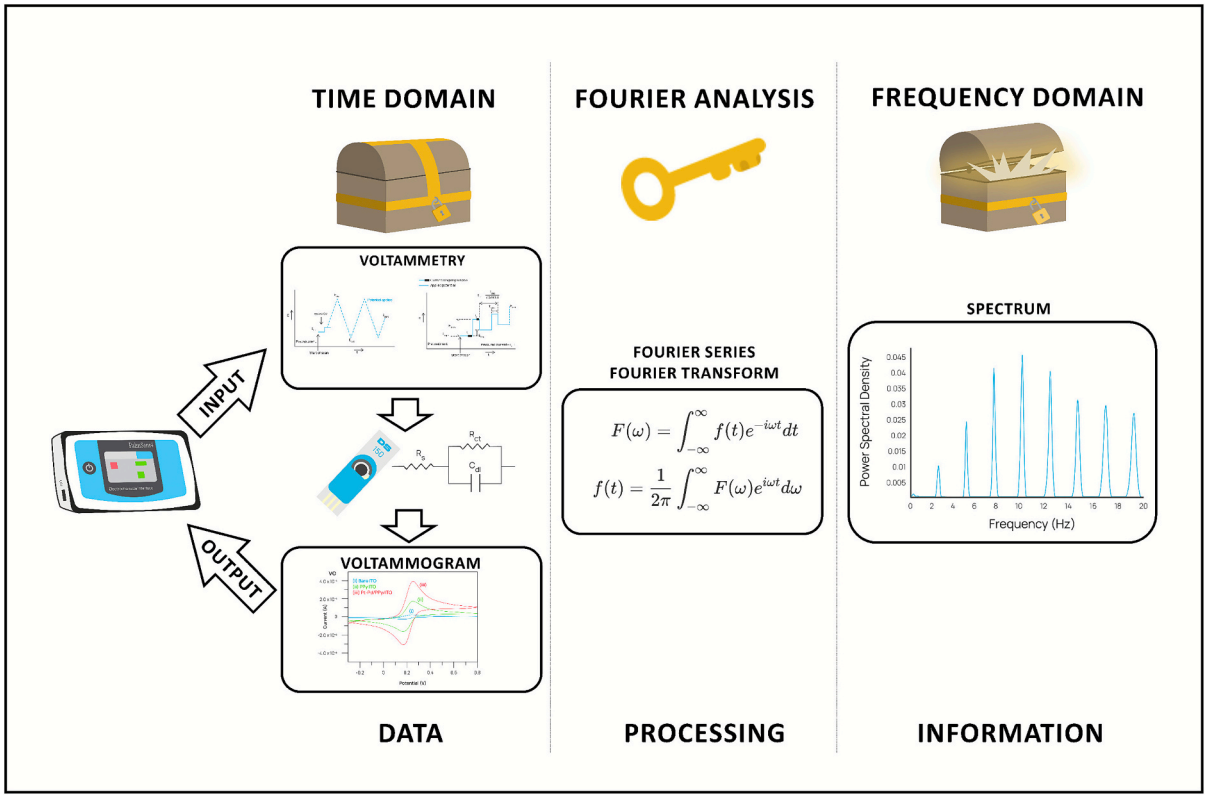

Fig. 1. (Graphical Abstract): Fourier analysis illustrated as the transformation of electrochemical time-domain signals into frequency-domain spectra. Faradaic and capacitive components are separated through signal processing to enhance measurement clarity.

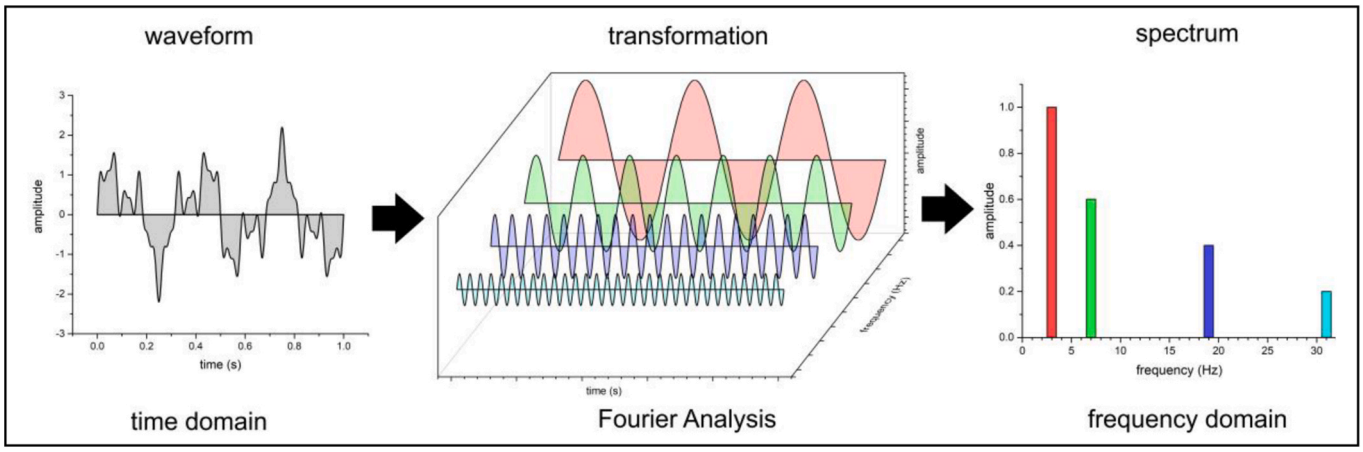

Fig. 2. Fourier analysis illustrated as decomposition of a time-domain waveform into its frequency-domain spectrum. Sinusoidal components combine to reconstruct the original signal.

3. Results and discussion

3.1. Response layer (output): AC voltammetry as a probe of frequency-resolved faradaic and non-faradaic processes

To ground the framework experimentally, ACV probes electrochemical behaviour by superimposing a small sinusoidal perturbation onto a linear potential sweep, enabling frequency-resolved observation of the system response. Unlike EIS, which requires small perturbations and steady-state conditions, ACV provides spectral insight during dynamic voltammetric scans. While wavelet-based methods can capture non-stationary features, the Fourier-based framework adopted here offers a simpler and broadly applicable route for analysing global frequency-dependent behaviour using standard voltammetric protocols under the assumption of linear time invariance (LTI).

3.1.1. Waveform structure and experimental parameters in AC voltammetry

Fig. 3 shows the ACV potential waveform, composed of the sum of a DC component (a linear sweep) and a sinusoidal AC component.

The small AC amplitude enables simultaneous analysis of faradaic and non-faradaic responses. The frequency (f) of the superimposed sine wave critically influences the relative contributions of the two responses. Maintaining a sufficiently slow scan rate allows the sinusoidal perturbation to dominate the system response, thereby reducing the influence of the underlying sweep and providing quasi-stationary conditions consistent with piecewise-LTI behaviour.

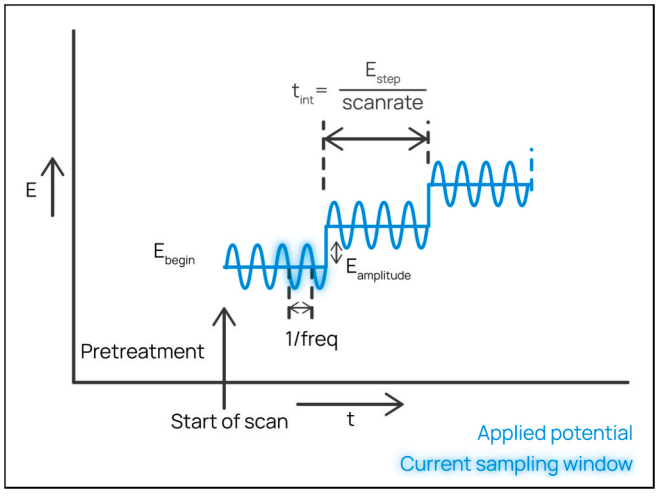

Fig. 3. AC voltammetry (ACV) waveform composed of a linear DC sweep and superimposed sinusoidal perturbation.

3.1.2. Benzenediol detection under variable frequency: suppression of capacitive currents to unmask faradaic signals

To investigate the frequency response of the electrochemical system during benzenediol detection, we performed ACV with a scan rate of 10 mV s^{-1}, an AC amplitude of 10 mV (RMS), a potential step of 10 mV, and voltage limits between 0 V to 1 V versus quasi-reference Ag electrode. We examined the effect of varying the AC frequency from 3 Hz to 2000 Hz using this setup, and the results are shown in Fig. 4.

At lower frequencies, distinct oxidation peaks [15,16] are observed. As frequency increases, the overall current rises. Notably, the background current (predominantly capacitive) increases proportionally with applied frequency.

As a result, the faradaic oxidation peaks of the benzenediols become progressively less prominent and are overwhelmed at higher frequencies by the capacitive current. To further examine this degradation, the Fast Fourier transform (FFT) [17] was applied to the ACV output data. The resulting spectra, shown in Fig. 5a, display sharp, well-localised peaks at the imposed excitation frequencies with no additional harmonic

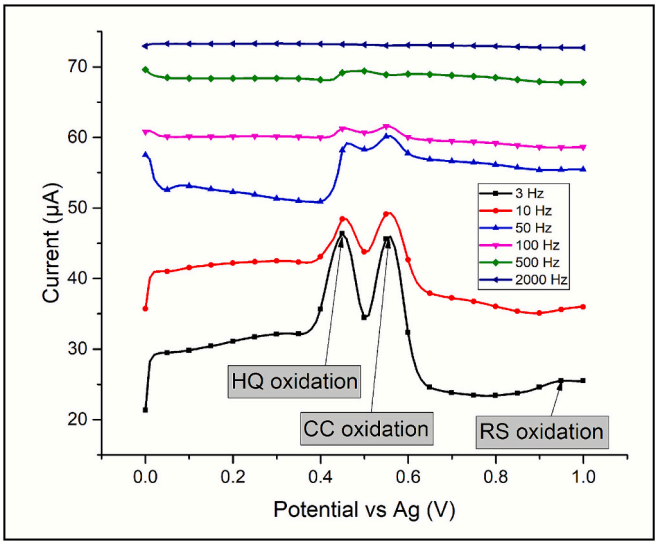

Fig. 4. AC voltammograms of benzenediols (1 mM catechol, 1 mM resorcinol and 1 mM hydroquinone in 1 M HCl) from 3 Hz to 2000 Hz; increasing frequency boosts capacitive current and progressively masks faradaic peaks.

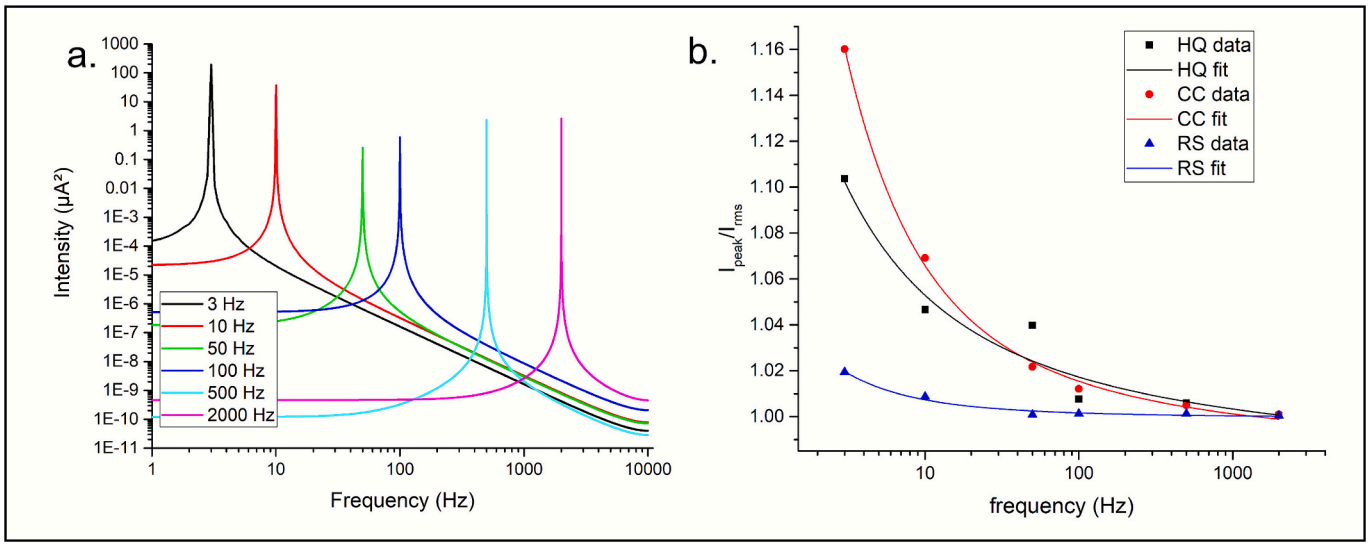

Fig. 5. (a) Fast Fourier transform spectra of ACV outputs, showing recovery of excitation frequencies and the absence of spurious harmonics, confirming linear time-invariant behaviour. (b) Peak-to-RMS current ratios decline with frequency, reflecting reduced faradaic clarity. Inverse logarithmic fits are included to guide the eye.

components. The FFT thus faithfully recovers in the output stage the exact frequencies introduced at the input, providing strong evidence of LTI system behaviour. In parallel, the peak-to-RMS current ratio (detailed in Eq. S15 in Supplementary Section 3.5.5) was calculated for each analyte across the frequency range of 3 Hz to 2000 Hz. This ratio quantifies signal prominence relative to background and, as shown in Fig. 5b, decreases systematically with frequency, reflecting the progressive loss of faradaic clarity due to capacitive effects. Together, the FFT spectra and the peak-to-RMS analysis reveal a consistent correlation between excitation frequency and signal degradation, confirming the utility of the frequency-domain framework for diagnosing the onset of capacitive masking.

These results highlight the challenge of detecting faradaic processes at high frequencies due to dominant capacitive currents. Selecting an appropriate frequency is therefore critical to balance analyte sensitivity and minimise interference from capacitive currents, allowing for a clearer observation of the redox processes of interest. Although both faradaic and capacitive processes are frequency-dependent, their relative dominance shifts with frequency, allowing selective enhancement or suppression of signal components through tuning. These frequency-dependent, qualitative trends indicate that the electrochemical cell itself imposes a structured response, largely independent of analyte identity, and thus provide the experimental foundation for the framework developed in the following sections.

3.2. *Transfer function (system): modelling frequency-dependent capacitive and faradaic current components*

Building on the ACV output-stage observations, the next section examines the electrochemical system through an equivalent circuit model that translates these empirical frequency trends into a formal description of interfacial behaviour.

To understand how frequency affects electrochemical currents, we model the system using a modified Randles circuit, shown in Fig. 6. In this equivalence, the charge transfer resistance (R_{ct}) represents electron transport across the electrode–electrolyte interface, encapsulating the kinetics of redox reactions. The Warburg element [18] (Z_w) accounts for semi-infinite linear diffusion of species to and from the electrode, reflecting mass-transport limitations. The double-layer capacitance [19] (C_{dl}) describes the charging and discharging of the interfacial electrolyte layer, i.e. non-faradaic contributions. The solution resistance (R_s) represents the ionic conduction through the electrolyte. Taken together,

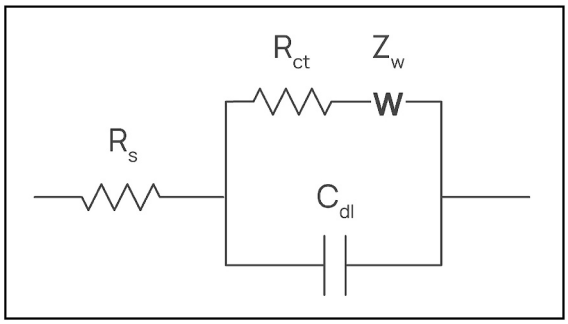

Fig. 6. Modified Randles equivalent circuit used to model the electrochemical cell comprising a solution resistance (R_s), a charge transfer resistance (R_{ct}) to model electron transfer in series with a Warburg element (Z_W) to model mass transport, and a double-layer capacitance (C_{dl}), representing electrolytic charging and discharging.

these circuit elements form a simplified analogue that captures the essential processes of electron transfer, mass transport, and double-layer charging. The Randles circuit is used here as a mechanistic abstraction layer: it consolidates the frequency response into discrete components agnostic of analyte-specific mechanisms, and enabling a general interpretation of frequency effects across electrochemical systems. By deconvolving charge transfer, double-layer charging and diffusion into standalone frequency-dependent components, the Randles circuit formalises the empirical observations from AC voltammetry and establishes the mathematical scaffold for spectral analysis.

The electrical double layer is formed at the interface between the electrode and the electrolyte solution, emulating a capacitor that stores charge. Double-layer charging and discharging contributes to the non-faradaic (capacitive) current (I_C) through the C_{dl} branch in Fig. 6. The non-faradaic current from double-layer [20] charging increases proportionally with the frequency of the applied AC signal, as shown in Eq. (1).

$$\boldsymbol{I_C(\omega) = \omega C_{dl} V_C(\omega)} \tag{1}$$

where I_C (A) is the non-faradaic or capacitive current, V_C (V) is the voltage across the double layer, C_{dl} (F) is the double-layer capacitance and $\boldsymbol{\omega = 2\pi f}$ (rad s^{-1}) is the angular frequency [f (Hz) is the linear frequency].

Simplifying Eq. (1),

$$|I_C(\omega)| \propto \omega \tag{1.1}$$

$$\angle I_C(\omega) \rightarrow 90^\circ \text{ or } \frac{\pi}{2} \tag{1.2}$$

The faradaic current (I_F) through the path containing R_{ct} and Z_W in Fig. 6 arises from electron transfer between the electrode and chemical species leading to redox reactions. The rate of these reactions is influenced by both the electrode potential and the kinetics of the electron transfer. Reaction kinetics [21] and the diffusion [22] of reactants to the electrode primarily govern the faradaic current, which also depends on the frequency. However, its frequency dependence is different from that of the capacitive current as shown in Eq. (2).

$$I_F(\omega) = \frac{V_F(\omega)}{R_{ct} + Z_W(\omega)} \tag{2}$$

where, I_F (A) is the faradaic current, V_F (V) is the voltage across the series combination of the charge transfer resistance R_{ct} (Ω) and the Warburg impedance Z_W (Ω).

R_{ct} represents the opposition to electron transport between the electrode and the redox species and is frequency-invariant.

Z_W represents the diffusion limitation, i.e., the resistance to mass transport of the redox species to/from the electrode and is defined in Eqs. (2.1) and (2.2).

$$|Z_W| = \frac{\sigma}{\sqrt{\omega}} \tag{2.1}$$

$$\angle Z_W = -45^\circ \text{ or } -\frac{\pi}{4} \tag{2.2}$$

where σ ($\Omega\ s^{-0.5}$) is the Warburg coefficient.

When $\omega \rightarrow 0$, $Z_W \gg R_{ct}$,

$$I_F = \frac{V_F\sqrt{\omega}}{\sigma} \tag{2.3}$$

Simplifying Eq. (2.3),

$$|I_F| \propto \sqrt{\omega} \tag{2.4}$$

$$\angle I_F \rightarrow 45^\circ \text{ or } \frac{\pi}{4} \tag{2.5}$$

When $\omega \rightarrow \infty$, $Z_W \ll R_{ct}$,

$$|I_F| = \frac{V_F}{R_{ct}} \tag{2.6}$$

$$\angle I_F \rightarrow 0^\circ \tag{2.7}$$

Fig. 7 visually consolidates the above equations on how redox and capacitive current magnitudes vary with frequency. In physical terms, these relations describe how diffusion-controlled faradaic currents dominate at low frequencies, while capacitive charging increasingly governs the response at higher frequencies, leading to the crossover frequency highlighted at the intersection of the two current curves.

Eqs. (1.1) through (2.7) and Fig. 7 show that:

1. The non-faradaic current increases proportionally with frequency. At regimes where this current is dominant the phase should be tending to 90° or $\frac{\pi}{2}$. In electrochemical terms, this reflects the charging and discharging of the double layer, which behaves as a capacitor. Within physical limits, the capacitive charging and discharging current is therefore a linear function of the excitation frequency.
2. Faradaic current increases with the square root of frequency at low ω, before becoming essentially frequency-invariant at higher values. Electrochemically, this means that at low frequencies, the dominant limitation is mass transport (diffusion of analyte to the electrode) which should be visible in the phase tending towards 45° or $\frac{\pi}{4}$. As frequency rises, diffusion constraints are progressively overcome until charge transfer becomes the bottleneck, beyond which further increases in frequency no longer influence the system which should reflect in the phase tending to 0°.

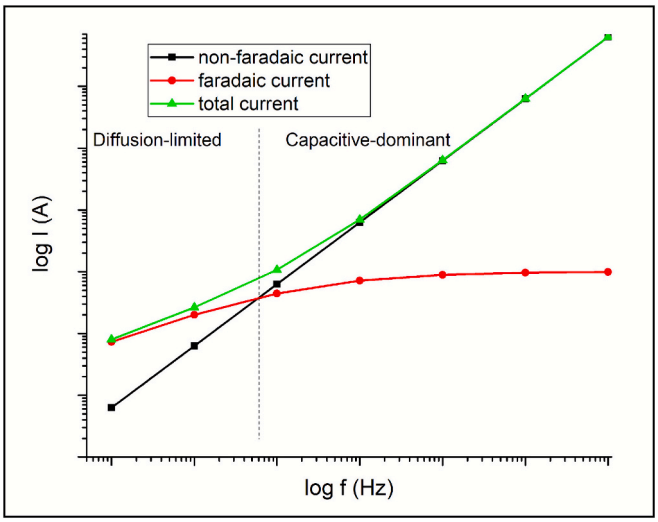

Fig. 7. Log–log illustration comparing faradaic and capacitive current magnitudes as functions of frequency, based on the equivalent circuit model. Highlights the crossover point where capacitive current begins to dominate and guides optimal frequency selection.

This presents a trade-off: at low frequencies, faradaic signals are diffusion-limited, whereas at high frequencies, capacitive currents dominate and mask the faradaic response.

Together, these relationships confirm that both the amplitude and the phase of the electrochemical system evolve predictably with excitation frequency. The Randles circuit therefore provides a reliable mathematical description of frequency-structured electrochemical behaviour, linking current magnitude and phase to the dominant transport and interfacial processes, and setting the stage for analysis of how excitation waveforms themselves encode this frequency structure.

3.3. Excitation characterisation (input): spectral analysis of canonical voltammetric waveforms

Having established the system's frequency response, the discussion now moves upstream to the input stage, where electrochemical techniques operate by applying time-varying potential waveforms that each carry their own frequency signature defined by shape, period and symmetry. Together, these techniques can be viewed as a single methodological family derived from LSV, with CV adding a reversed scan that returns to the initial potential and cycles between the vertices, DPV superimposing a train of rapid potential pulses onto a slow baseline LSV, and SWV modulating the LSV with a square-wave signal, each producing a distinctive harmonic distribution.

The measured output current is a function of both the input waveform and the electrochemical system's frequency response. Consequently, its spectrum reflects both the temporal evolution of the driving signal and the system's underlying transfer characteristics. Fourier analysis provides a practical means to obtain the spectra of these input signals, revealing how waveform design accentuates or attenuates specific frequency regions.

The relative amplitude and distribution of spectral components determine how strongly different electrochemical processes are stimulated. Recognising this intrinsic frequency structure clarifies the characteristic strengths of each voltammetric approach: some favour

mechanistic simplicity, whereas others gain sensitivity through deliberate modulation and sampling. Viewed in the frequency domain, these diverse techniques converge into a unified description where differing time-domain parameters coalesce into directly comparable information.

Figs. 8–11 summarise some examples of canonical voltammetric waveforms and their corresponding spectra obtained using Fourier series (FS) decomposition, illustrating how waveform geometry determines harmonic content and spectral distribution.

3.3.1. Linear sweep voltammetry: harmonic complexity in sawtooth potential sweeps

For a LSV with the following parameters: $E_{begin} = 0$ V, $E_{end} = 1$ V, and scan rate = 10 mV s^{-1}, Fig. 8 shows the waveform and the spectrum.

In LSV, the potential increases linearly between fixed vertices at a constant rate. The corresponding spectrum reveals both odd and even harmonics (f_0, $2f_0$, $3f_0$, …) of the 10 mHz fundamental frequency along with a strong DC component at 0 Hz, reflecting the waveform's amplitude asymmetry.

3.3.2. Cyclic voltammetry: odd harmonic dominance in triangular waveforms

For a CV with the following parameters: $E_{begin} = 0$ V, $E_{vertex1} = 1$ V, $E_{vertex2} = 0$ V, and scan rate = 10 mV s^{-1}, Fig. 9 shows the waveform and the spectrum.

In CV, the potential sweeps linearly between two limits and then reverses to form a triangular profile. The corresponding spectrum contains only odd harmonics (f_0, $3f_0$, $5f_0$, …) of the 5 mHz fundamental and exhibits a faster decay of higher-order harmonics than LSV. A DC component arises from amplitude asymmetry in the waveform.

3.3.3. Differential pulse voltammetry: harmonic complexity and sinc-shaped spectra from pulse trains

For a DPV with the following parameters: $E_{begin} = 0$ V, $E_{end} = 1$ V, scan rate = 10 mV s^{-1}, pulse amplitude = 30 mV, pulse duration = 50 ms, voltage step = 10 mV, and pulse interval = 1 s, Fig. 10 shows the waveform and the spectra.

In DPV, a linear potential sweep is combined with a high-frequency pulse train, producing two distinct spectral components: a low-frequency sawtooth and a high-frequency sinc-shaped ($\frac{\sin\pi t}{\pi t}$) envelope. The 5 % duty cycle used in this illustration introduces nulls at every twentieth harmonic (f_0, $20f_0$, $40f_0$, …), consistent with the reciprocal relation between duty cycle and harmonic spacing.

3.3.4. Square wave voltammetry: high harmonic distortion from square wave superposition on a linear sweep

For a SWV with the following parameters: $E_{begin} = 0$ V, $E_{end} = 1$ V, scan rate = 10 mV s^{-1}, square-wave amplitude = 30 mV, square-wave period = 0.1 s (fundamental frequency = 10 Hz), and voltage step = 10 mV, Fig. 11 shows the waveform and the spectra.

In SWV, a linear potential ramp is superimposed with a square-wave modulation, generating two spectral components: a low-frequency ramp and a high-frequency square-wave contribution. The latter displays harmonic peaks at odd integer multiples (f_0, $3f_0$, $5f_0$, …) consistent with the 50 % duty cycle that suppresses even harmonics. SWV therefore provides a useful mathematical contrast to the DPV example in this study, where a 5 % duty cycle produced nulls at every twentieth harmonic. The square wave's slower harmonic decay yields stronger higher-order contributions, while the waveform's amplitude symmetry eliminates the DC component.

3.3.5. Fast Fourier transform spectra of canonical voltammetric waveforms

The FS spectra presented earlier describe idealised, infinitely periodic waveforms. To complement these, the FFT was applied to the same canonical waveforms described in Sections 3.3.1 to 3.3.4. These quasi-simulations illustrate how the signals would appear if the waveforms were fed directly into a spectral analyser.

The simulated spectra in Fig. 12 highlight the practical challenges that arise when moving from mathematical decomposition to empirical analysis. The quality of the spectra depends critically on parameters defined by the user, such as the sampling frequency and the bin resolution. While oversampling can in principle improve fidelity, it also generates redundant data and brings optimisation into the conversation. Improper binning can introduce artefacts. For example, in CV, the FFT spectrum exhibits weak even harmonics, which are absent from the FS spectrum and result from finite sampling and binning artefacts. For DPV, the FFT spectrum combines both contributions observed earlier: the low-frequency sweep component and the high-frequency pulse train. These appear as one spectrum with the sinc-shaped envelope of the high frequency pulses being dominant, illustrating how composite waveforms yield complex spectral distributions. In SWV, the FFT correctly shows the absence of even harmonics, but lobes appear around the odd harmonics due to binning artefacts, unlike the sharp lines observed in the Fourier series decomposition.

Together, these examples illustrate the phenomenon of spectral leakage [23], which arises because the FFT operates on finite, discrete

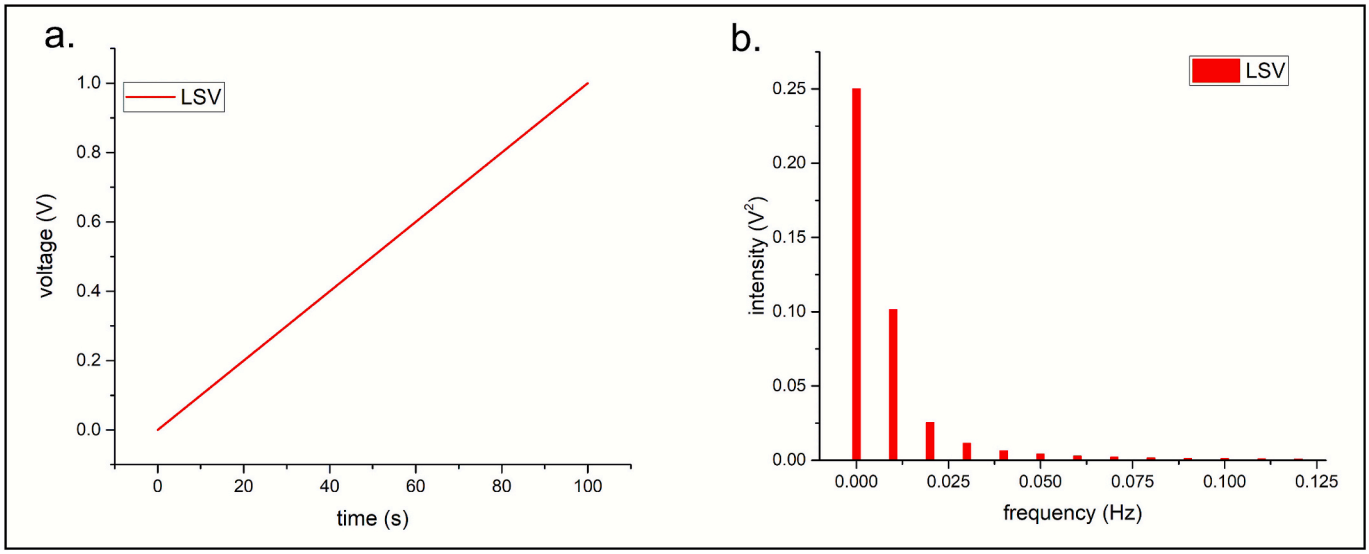

Fig. 8. Linear Sweep Voltammetry (LSV): (a) time-domain sawtooth waveform; (b) Fourier series spectrum showing both odd and even harmonics of the 10 mHz fundamental, with a strong DC component.

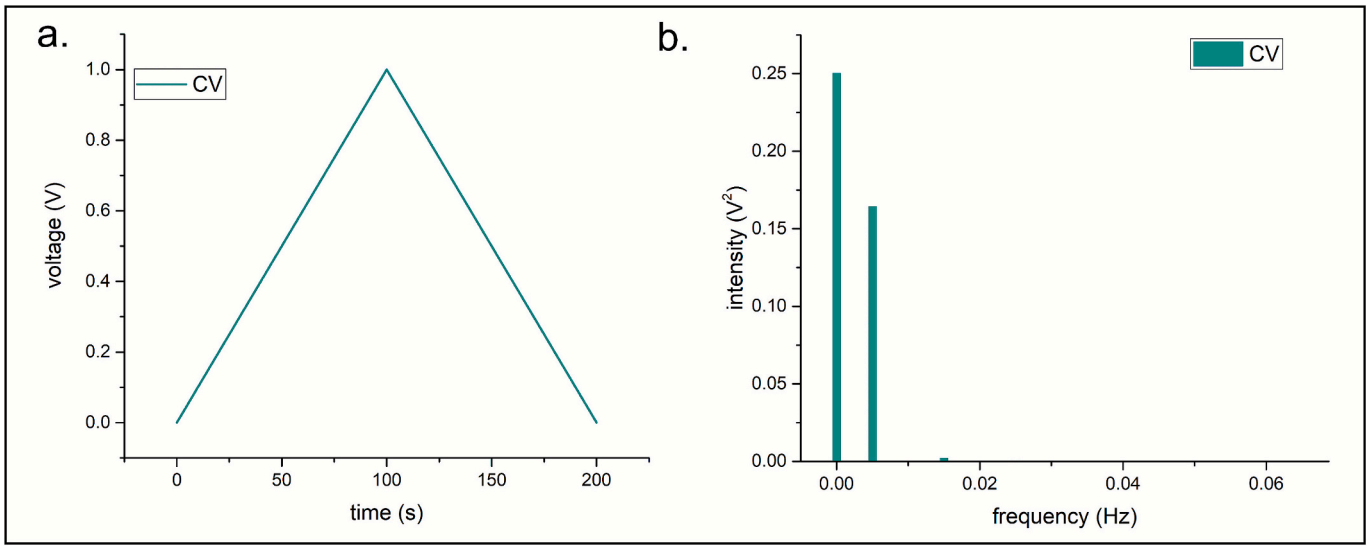

Fig. 9. Cyclic Voltammetry (CV): (a) triangular waveform; (b) Fourier series spectrum containing only odd harmonics (5 mHz fundamental), with rapid harmonic decay, and a DC component caused by amplitude asymmetry.

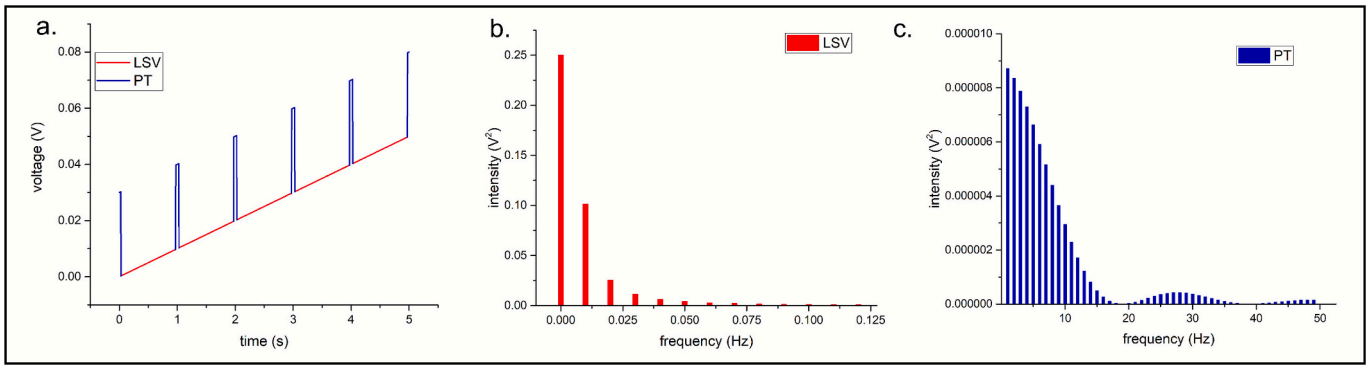

Fig. 10. Differential Pulse Voltammetry (DPV): (a) composite sawtooth plus pulse-train waveform (first 5 s shown); (b) low-frequency sawtooth Fourier series spectrum; (c) sinc-modulated pulse Fourier series spectrum with nulls at every 20th harmonic (5 % duty cycle).

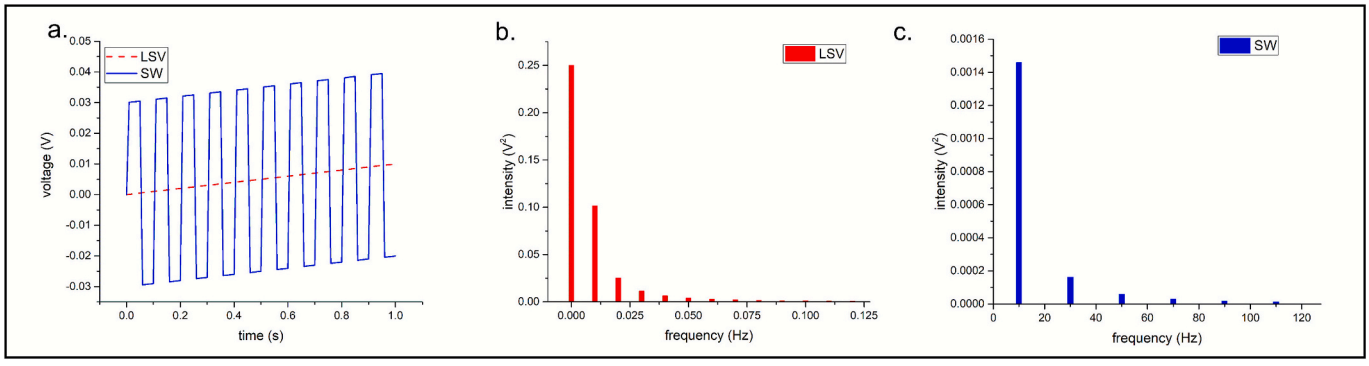

Fig. 11. Square Wave Voltammetry (SWV): (a) sawtooth plus square wave (first 1 s shown); (b) low-frequency sawtooth Fourier series spectrum; (c) square-wave Fourier series spectrum with odd harmonics only and slower decay.

signals rather than infinitely periodic, continuous ones. Unlike FS analysis, which assumes perfect periodicity and yields clean harmonic structure, the FFT outputs are susceptible to leakage, artefacts, and noise. Recognising these differences highlights that the discrete, finite nature of real signals broadens and redistributes spectral energy, yet the underlying harmonic relationships revealed by Fourier-series analysis remain embedded within experimental spectra. Without the knowledge of these effects, practitioners may misinterpret the FFT outputs. By placing the ideal mathematical FS results alongside the quasi-simulated FFT spectra, this framework informs readers what features to expect and what artefacts to avoid when applying spectral analysis in practice. Fourier decomposition shows that canonical voltammetric waveforms are inherently frequency-coded, while FFT artefacts can even collapse distinct techniques into deceptively similar spectra. Quantitative

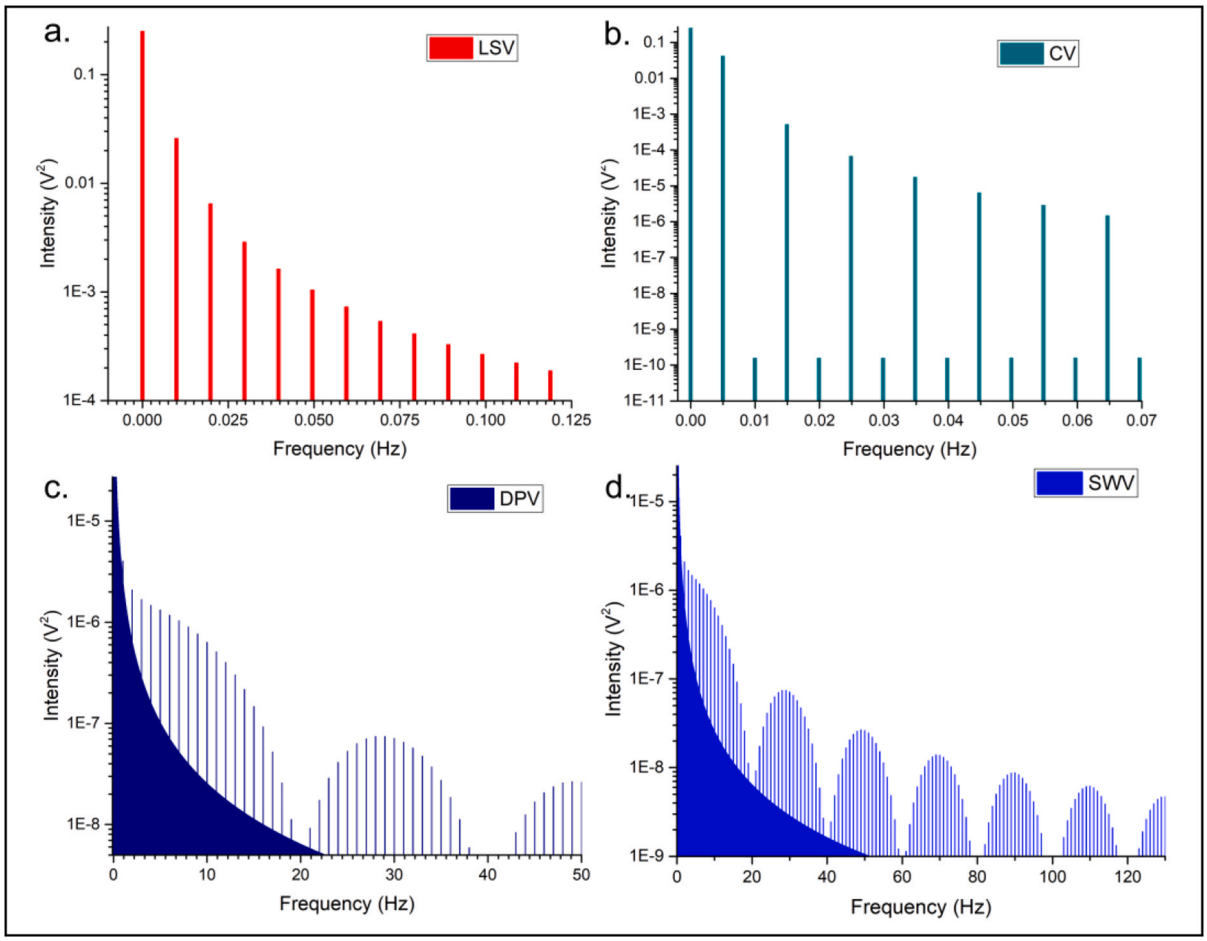

Fig. 12. Fast Fourier transform spectra of canonical voltammetric waveforms: (a) linear sweep voltammetry, (b) cyclic voltammetry, (c) differential pulse voltammetry, (d) square wave voltammetry. Quasi-simulations highlight artefacts from finite-sampling, binning effects, and spectral leakage that are absent from the Fourier series decompositions.

spectral descriptors are therefore essential for reliable discrimination and design.

3.4. From waveform tuning to electrochemical measurement design: a unified frequency-structured framework

ACV observations on capacitive and faradaic frequency dependence offer a framework for optimising voltammetric parameters to enhance faradaic signals and reduce capacitive interference. As discussed in Section 3.3, although techniques such as LSV, CV, DPV, and SWV operate in the time domain, their waveforms contain a spectrum of frequency components that stimulate faradaic and non-faradaic processes differently.

Across all voltammetric modes, frequency tuning governs the balance between diffusion-limited and capacitive-dominated regimes. In LSV and CV, slower scan rates reduce capacitive background and sharpen redox peaks, whereas excessively low rates lead to diffusion limitation. In DPV and SWV, longer pulse widths, intervals, or longer periods for square waves similarly suppress capacitive interference but must be optimised to maintain adequate diffusion. Overall, parameter selection represents a simple trade-off: too high a frequency amplifies capacitive currents, too low a frequency restricts mass transport.

This frequency-dependent behaviour links waveform design directly to measurement clarity and defines practical boundaries for each technique. For example, as seen from the SWV spectra in Section 3.3.4, choosing 10 Hz as the fundamental frequency seems reasonable. However, ACV results show a significant difference between 3 Hz and 10 Hz. At 10 Hz, RS oxidation is completely masked by the capacitive current, while at 3 Hz it remains faintly visible. The peaks for HQ and CC, while still visible at 10 Hz, are much better defined at 3 Hz. The square wave in SWV introduces the fundamental frequency along with a cascade of odd harmonics (30 Hz, 50 Hz, 70 Hz, …), increasing total frequency content and further exacerbating capacitive interference. At frequencies above 100 Hz, the peaks become only faintly discernible, blending into the error margins and rendering them nearly indistinguishable from the background. These results also show that an ACV frequency of 3 Hz sufficiently overcomes diffusion limitations, revealing distinct oxidation peaks over the capacitive background.

This frequency dependence also explains why different voltammetric techniques display varying sensitivities to the same electrochemical system. For instance, chronoamperometry effectively drives the excitation frequency towards zero, thereby suppressing capacitive currents almost entirely. DPV and SWV, on the other hand, introduce higher-frequency components and thus more capacitive current than cyclic voltammetry. Yet this apparent drawback is exploited at the output stage: potentiostats sample the current signal at the end of each pulse (as shown in the Supplement in Fig. S2), when the capacitive transient has decayed, allowing the residual faradaic current to be captured with sharper clarity. In this way, DPV can outperform CV in apparent sensitivity, even though its underlying frequency content is less favourable.

To extend the qualitative comparison of Fourier series and FFT spectra, we quantified waveform frequency characteristics using a set of spectral descriptors. These metrics were computed for LSV, CV, DPV, and SWV to characterise how signal energy is distributed across

frequencies. Table 1 summarises four key spectral parameters: spectral centroid, bandwidth, flatness, and low-frequency power fraction (below 30 Hz) comparing the theoretical FS and practical FFT data. Detailed formulations are provided in Supplementary Eqs. S11 to S14.

LSV and CV show extremely low centroids and bandwidths, while DPV and SWV show relatively low centroids, and their bandwidths are significantly wider due to the high-frequency components. The waveforms show generally flat spectra, and all demonstrate that most of their power lies below 30 Hz, chosen as a conservative soft limit since the ACV results show distinguishable peaks up to 50 Hz. Differences between the theoretical (FS) and practical (FFT) values reflect spectral leakage and finite sampling, as discussed in Section 3.3.5. The spectral metrics also highlight the pitfalls of applying the FFT without sufficient rigour. The practical spectra of both DPV and SWV yield identical values across all metrics, effectively implying that the two waveforms are the same. The FS results, however, show that their spectral structures differ markedly, demonstrating that uncritical use of the FFT can obscure essential distinctions between voltammetric techniques.

Collectively, these findings position spectral interpretation as a core tool for selecting parameters, designing sensors, and understanding mechanisms. Insights from ACV, which clearly showed how capacitive currents can mask faradaic signals above certain frequencies, directly inform the selection of time-domain parameters. By understanding that lower frequency components limit diffusion and higher frequency components tend to amplify capacitive effects, researchers can strategically select parameters in LSV, CV, DPV, and SWV to enhance the faradaic response. Careful time-domain parameter selection is essential for achieving adequate sensitivity in frequency-dependent electrochemical sensing. Taken together, the empirical ACV results, circuit model and waveform spectra converge on the same message: electrochemical measurement is inherently frequency-structured, and this approach offers a practical route to tune experiments for faradaic clarity.

To support practical application, Table 2 summarises the key frequency-domain features of common voltammetric waveforms and offers guidance on parameter choices to enhance faradaic signal detection by aligning waveform design with spectral behaviour.

4. Limitations of Fourier analysis in electrochemistry

The framework presented here is metrological rather than analytical in scope, addressing the structure and interpretation of electrochemical signals generally, independent of the underlying system and its corresponding specificities.

4.1. Noise

Electrochemical signals often contain noise from multiple sources that Fourier analysis cannot fully eliminate [24]. While it can help identify certain noise frequencies, when noise overlaps with the signal of interest, it can distort the spectra and hinder accurate interpretation of electrochemical processes [25].

Table 1
Spectral metrics of canonical voltammetric waveforms. Values describe how signal energy is distributed across frequencies and highlight their suitability for resolving frequency-specific redox and capacitive behaviours.

Waveform		Centroid (mHz)	Bandwidth (mHz)	Flatness	Low-frequency power fraction: Power below 30 Hz (%)
LSV	**Theoretical**	9.36	22.93	0	100
	Practical	4.42	24.13	0	100
CV	**Theoretical**	2.07	2.77	0	100
	Practical	0.75	1.95	0	100
DPV	**Theoretical**	10.64	142.4	0	100
	Practical	10.29	578.81	0	100
SWV	**Theoretical**	89.06	2137.61	0	99.92
	Practical	10.29	578.81	0	100

Table 2
Summary of waveform types, spectral characteristics, and tuning strategies for improving faradaic signal clarity.

Technique	Waveform model	Spectral insight and optimisation	Tuning guidance
LSV	Sawtooth wave	High low-frequency power; moderate scan rate balances redox clarity and time resolution	Lower scan rate to reduce capacitive background
CV	Triangle wave	Narrowband, odd harmonics; low centroid and flatness support mechanistic interpretation	Lower scan rate to enhance peak definition
DPV	Sawtooth + pulse train	Broad spectrum with clustered harmonics; optimise pulse interval to preserve peak shape	Use longer pulse width and interval for better resolution
SWV	Sawtooth + square wave	High centroid and flatness; reducing frequency improves faradaic visibility	Lower modulation frequency to minimise background interference
ACV	Sawtooth + sine wave	Spectral response depends on excitation; use peak-to-RMS to select optimal frequency	Adjust excitation frequency to isolate faradaic signal

4.2. Non-ideal conditions and non-linearities

Fourier analysis assumes linear systems but electrochemical systems can exhibit non-linear behaviour under non-ideal conditions [26]. Non-linearities introduce spurious harmonics that complicate analysis [27]. Uncompensated resistance [28] and frequency-dependent capacitive behaviour (capacitive dispersion) [29] contribute to these non-linearities.

4.3. Complexity of electrode kinetics

Intricate multi-step mechanisms [30] in electrochemical reactions often produce complex frequency responses. While Fourier analysis provides valuable information, researchers often need complementary techniques and modelling to decompose these complex responses and fully understand the underlying kinetics.

4.4. Hardware considerations

The present analysis treats the electrochemical cell as a continuous-time system, an assumption justified because electrochemical time constants are far longer than the sampling intervals of modern potentiostats. Although a fully discrete treatment using Z-transforms and difference equations could, in principle, be applied, it lies beyond the scope of this work. A comparison of analogue and digital signal modes using the same potentiostat has been discussed elsewhere [31], where quantisation and staircase inputs were shown to influence double-layer charging. Under typical experimental conditions, treating the system as continuous remains accurate and widely applicable. Fig. 13 illustrates the practical distinction between analogue and digital CV waveforms, where the exaggerated staircase shape of digital signals reflects quantised sampling.

4.5. Time resolution and stationarity

Fourier analysis assumes stationary signals and involves a trade-off between frequency and time resolution. Electrochemical systems are

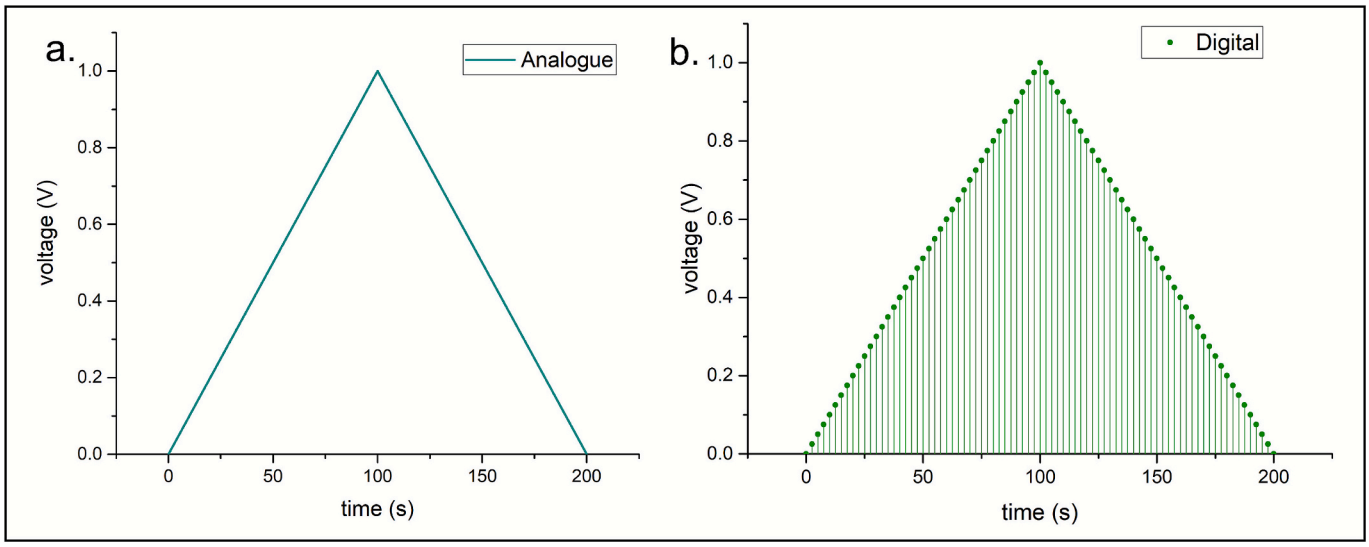

Fig. 13. CV waveforms in (a) analogue and (b) digital modes. Analogue mode produces a continuous triangular ramp, digital mode yields a quantised staircase approximation.

generally stochastic and can be non-stationary, and researchers must use specialised approaches [32] when applying Fourier analysis to systems with time-varying signals. While Fourier analysis provides valuable frequency-domain insights for stationary or quasi-stationary electrochemical signals, future studies could apply wavelet transforms [33] to systems with significant non-stationarity, using localised time–frequency analysis to gain additional insights.

5. Broader applications and future work

Fourier and frequency-domain approaches extend well beyond sensing [34] and can inform studies of corrosion [35], batteries [36], fuel cells [37], and electrocatalysis, where frequency-dependent transport and charge transfer also govern performance. Comparable behaviour has been observed in aniline electropolymerisation, where lower scan rates produced porous, high-capacitance films while higher rates yielded compact, resistive deposits [38]. Such examples highlight a common principle: excessive high-frequency content prioritises non-faradaic processes, whereas low-frequency components tend to enhance functional efficiency. Extending the present framework to these broader contexts could therefore support more rational design of electrochemical systems and materials.

6. Conclusion

This study demonstrates that electrochemical measurement is inherently frequency-structured. The behaviour of the electrochemical interface cannot be fully understood in the time domain alone, and frequency-domain analysis provides the complementary view required to separate and quantify the intertwined faradaic and capacitive processes.

AC voltammetry (ACV) established the experimental foundation for this framework. By varying the excitation frequency, ACV revealed that capacitive currents increase proportionally with frequency while faradaic currents become progressively masked. This behaviour was reproducible across three benzenediols with distinct redox chemistries, confirming that the phenomenon originates from the measurement system rather than the analytes.

A modified Randles equivalent circuit provided the mathematical basis for interpreting this response. Through its frequency-dependent elements, which represent charge transfer, diffusion and double-layer capacitance, the model explains how the relative magnitudes of faradaic and capacitive currents evolve with frequency. It defines the balance between diffusion-limited and capacitance-dominated regimes and clarifies the transition between them.

Fourier and spectral analysis of canonical voltammetric waveforms extended these insights into a general framework. The harmonic structure of linear sweep, cyclic, differential pulse and square wave voltammetry links waveform geometry directly to frequency content and therefore to the visibility of faradaic signals. Quantitative spectral descriptors such as the centroid, bandwidth, flatness and low-frequency power fraction provide practical metrics for comparing and optimising waveform parameters.

Together, these three components form a coherent and logical methodology for interpreting and designing electrochemical measurements. The framework guides the optimal selection of time-domain parameters to reduce capacitive interference, enhance faradaic visibility and improve measurement interpretability.

Although demonstrated here using benzenediol detection on Pt/C-modified screen-printed electrodes, the principles are broadly applicable to any system governed by convolved diffusion, charge-transfer and capacitive processes. Extending frequency-domain analysis to areas such as corrosion, electrocatalysis and energy storage can enable better insights into electrochemical system behaviours.

In summary, frequency-domain analysis provides a unified and robust approach to link electrochemical experimental design with interfacial dynamics. The study traces this relationship in reverse, from output spectra obtained by ACV, through system behaviour modelled by the modified Randles circuit, to input spectra defined by waveform geometry. This reverse progression mirrors the logic of signal analysis, connecting measurement, theory, and design within a single framework. By combining ACV results, equivalent circuit modelling and Fourier analysis, this work establishes a foundation for potential electrochemical methods that treat frequency not as a peripheral or specialist variable but as an intrinsic coordinate of electrochemical behaviour. Ultimately, this perspective reframes electrochemical measurement as a spectral science, where time-domain measurements are understood as projections of frequency-structured interfacial dynamics.

7. Experimental section: catalyst, sensor, analyte, and measurement setup

7.1. Catalyst preparation

The catalyst ink was prepared by dispersing 20 wt% Pt/C [platinum nanoparticles (2–3 nm) on Vulcan XC-72R (20–50 nm) support] sourced from FuelCellStore, in 0.995 ml of absolute ethanol. To this suspension, 5 µl of a 5 % Nafion solution in absolute ethanol (Sigma Aldrich) was added as a binder. The suspension was then ultrasonicated using a 500 W probe at 25 % amplitude for 2 min to ensure uniform dispersion. The ink was used immediately to prevent particle settling and agglomeration.

7.2. Sensor element fabrication

Sensor elements were fabricated using Metrohm DropSens DS150 screen-printed electrodes (SPE) with carbon working electrode (WE), platinum counter electrode (CE), and silver reference electrode (RE). The WE surface was cleaned with deionised water and ethanol, then dried on a hot plate maintained at 55 °C. 10 µl of catalyst ink was pipetted onto the WE on the hot plate to speed drying. Care was taken to isolate the CE and RE from deposition spill-over. The fabricated sensor elements were then stored in a dry, sealed container to prevent tarnishing of the silver contacts and RE. Each 10 µl aliquot of ink contained 10 µg of catalyst (1 mg/ml), of which 20 % was Pt, resulting in a theoretical metal loading of 2 µg per sensor element. Given the WE diameter of 4 mm, this corresponds to a Pt loading of approximately 160 ng mm^{-2} on the WE surface.

7.3. Analyte solution preparation

Analyte solutions of various concentrations were prepared by diluting stock solutions of each benzenediol. Catechol (CC), resorcinol (RS) and hydroquinone (HQ), all of analytical grade purity (>99 %) and purchased from Sigma Aldrich, were used. Stock solutions of each benzenediol (50 mM) were created by dissolving the analyte in 1 M HCl (prepared by diluting 37 % HCl) with stirring, aided by an ultrasonic bath. Working solutions were prepared by diluting the stock with 1 M HCl to reach target concentrations. For each measurement, 75 µl of the analyte solution was carefully dispensed onto the SPE surface, ensuring complete coverage of all three electrodes.

7.4. Instruments and electrochemical measurements

AC voltammetry (ACV) measurements were performed using a PalmSens4 potentiostat with the following parameters: scan rate: 10 mV s^{-1}; E_{ac}: 10 mV (root-mean-square value, RMS); E_{step}: 10 mV; E_{begin} = 0 V, E_{end} = 1 V (all vs quasi-reference Ag); frequency range: 3 Hz to 2000 Hz.

CRediT authorship contribution statement

Abhilash Krishnamurthy: Writing – review & editing, Writing – original draft, Visualization, Validation, Software, Methodology, Investigation, Formal analysis, Data curation, Conceptualization. **Kristina Žagar Soderžnik:** Validation, Supervision, Resources, Project administration, Methodology, Investigation, Funding acquisition.

Declaration of competing interest

The authors declare that they have no known competing financial interests or personal relationships that could have appeared to influence the work reported in this paper.

Acknowledgements

The authors gratefully acknowledge the Slovenian Research and Innovation Agency (ARIS) for their financial contribution to this work provided through grants: P2–0084 (Programme Nanostructured Materials), J2–1739 (High Performance Nanostructured Acrylamide Sensors), J2-3051 (SensePMC), and PR-09874 (Young Researcher Project). The authors also thank Pika Štefančič for her assistance with the graphical artwork.

Appendix A. Supplementary data

Supplementary data to this article can be found online at https://doi.org/10.1016/j.measurement.2025.119706.

Data availability

Data will be made available on request.

References

[1] A.J. Bard, L.R. Faulkner, H.S. White, Electrochemical methods: fundamentals and applications, John Wiley & Sons, 2022.
[2] V.D. Parker, Linear sweep and cyclic voltammetry, in: Comprehensive Chemical Kinetics, Elsevier, 1986, pp. 145–202.
[3] A.P. Brown, F.C. Anson, Cyclic and differential pulse voltammetric behavior of reactants confined to the electrode surface, Anal. Chem. 49 (11) (1977) 1589–1595.
[4] L. Ramaley, M.S. Krause, Theory of square wave voltammetry, Anal. Chem. 41 (11) (1969) 1362–1365.
[5] R.W. Newcomb, Analysis in the time domain, in: Circuit Analysis and Feedback Amplifier Theory, CRC Press, 2018, p. 9.
[6] P.M. Biesheuvel, S. Porada, J.E. Dykstra, The difference between Faradaic and non-Faradaic electrode processes, (2018), arXiv preprint arXiv:1809.02930.
[7] P.S. Singh, S.G. Lemay, Stochastic processes in electrochemistry, Anal. Chem. 88 (10) (2016) 5017–5027.
[8] S.O. Engblom, J.C. Myland, K.B. Oldham, Must ac voltammetry employ small signals? J. Electroanal. Chem. 480 (1–2) (2000) 120–132.
[9] T. Kadyk, Y. Sun, J. Kaur, A. Kulikovsky, M. Eikerling, Frequency response diagnostics of electrochemical energy devices, Curr. Opin. Electrochem. 42 (2023) 101378.
[10] A. Vretblad, A. Vretblad, Fourier analysis and its applications, Springer, New York, 2003.
[11] R.J. Marks, Handbook of Fourier analysis & its applications, Oxford University Press, 2009.
[12] Y. Katznelson, An introduction to harmonic analysis, Cambridge University Press, 2004.
[13] B.Y. Chang, S.M. Park, Electrochemical impedance spectroscopy, Annu. Rev. Anal. Chem. 3 (1) (2010) 207–229.
[14] A. Krishnamurthy, Z. Samardžija, Š. Trafela, A. Korent, S. Šturm, K.Ž. Soderžnik, Electrochemical detection of benzenediols using carbon-supported catalysts, Electrochimica Acta 493 (2024) 144389.
[15] M.A. Ghanem, Electrocatalytic activity and simultaneous determination of catechol and hydroquinone at mesoporous platinum electrode, Electrochem. Commun. 9 (10) (2007) 2501–2506.
[16] K. Ngamchuea, B. Tharat, P. Hirunsit, S. Suthirakun, Electrochemical oxidation of resorcinol: mechanistic insights from experimental and computational studies, RSC Adv. 10 (47) (2020) 28454–28463.
[17] W.T. Cochran, J.W. Cooley, D.L. Favin, H.D. Helms, R.A. Kaenel, W.W. Lang, P. D. Welch, What is the fast Fourier transform? Proc. IEEE 55 (10) (1967) 1664–1674.
[18] S.R. Taylor, E. Gileadi, Physical interpretation of the Warburg impedance, Corrosion 51 (9) (1995) 664–671.
[19] S. Westerlund, L. Ekstam, Capacitor theory, IEEE Trans. Dielectr. Electr. Insul. 1 (5) (1994) 826–839.
[20] B.B. Damaskin, O.A. Petrii, Historical development of theories of the electrochemical double layer, J. Solid State Electrochem. 15 (2011) 1317–1334.
[21] K.J. Vetter, Electrochemical kinetics: theoretical aspects, Elsevier, 2013.
[22] H. Züchner, N. Boes, Electrochemical methods for diffusion measurements, Berichte Der Bunsengesellschaft Für Physikalische Chemie 76 (8) (1972) 783–790.
[23] A. Breitenbach, Against spectral leakage, Measurement 25 (2) (1999) 135–142.
[24] A. Aballe, M. Bethencourt, F.J. Botana, M. Marcos, Wavelet transform-based analysis for electrochemical noise, Electrochem. Commun. 1 (7) (1999) 266–270.
[25] R.A. Cottis, Interpretation of electrochemical noise data, Corrosion 57 (3) (2001) 265–285.
[26] M.T. Koper, Non-linear phenomena in electrochemical systems, J. Chem. Soc. Faraday Trans. 94 (10) (1998) 1369–1378.
[27] K. Krischer, Nonlinear dynamics in electrochemical systems, Adv. Electrochem. Sci. Eng. 8 (2002) 89–208.

[28] K.B. Oldham, The effect of uncompensated resistance on the potential-step method of investigating electrochemical kinetics, J. Electroanalyt. Chem., 11(3) (1966), 171–187.
[29] T. Pajkossy, Impedance of rough capacitive electrodes, J. Electroanal. Chem. 364 (1–2) (1994) 111–125.
[30] M.C. Lefebvre, Establishing the link between multistep electrochemical reaction mechanisms and experimental Tafel slopes, in: Modern Aspects of Electrochemistry, Springer, US, Boston, MA, 2002, pp. 249–300.
[31] A. Krishnamurthy, K. Žagar Soderžnik, Influence of Potentiostat Hardware on Electrochemical Measurements, Sensors 24 (15) (2024) 4907.
[32] D. Griffin, J. Lim, Signal estimation from modified short-time Fourier transform, IEEE Trans. Acoust. Speech Signal Process. 32 (2) (1984) 236–243.
[33] P.M. Bentley, J.T.E. McDonnell, Wavelet transforms: an introduction, Electr. Commun. Eng. J. 6 (4) (1994) 175–186.
[34] D.W. Kimmel, G. LeBlanc, M.E. Meschievitz, D.E. Cliffel, Electrochemical sensors and biosensors, Anal. Chem. 84 (2) (2012) 685–707.
[35] R.H. Brown, R.B. Mears, The electrochemistry of corrosion, Trans. Electrochem. Soc. 74 (1) (1938) 495.
[36] K. Schmidt-Rohr, How batteries store and release energy: explaining basic electrochemistry, J. Chem. Educ. 95 (10) (2018) 1801–1810.
[37] S. Srinivasan, Fuel cells: from fundamentals to applications, Springer Science & Business Media, 2006.
[38] A. Kellenberger, D. Ambros, N. Plesu, Scan rate dependent morphology of polyaniline films electrochemically deposited on nickel, Int. J. Electrochem. Sci. 9 (12) (2014) 6821–6833.